Pergamon

Cement and Concrete Research, Vol. 28, No. 10, pp. 1429–1444, 1998

0008-8846/98 $19.00 + .00

PII S0008-8846(98)00108-2

EXPERIMENTAL STUDY OF THE MICROSTRUCTURAL INFLUENCE OF THE STRAIN-SOFTENING BEHAVIOR OF CEMENT MORTAR

R. Dasgupta,* J.C. Hay,* C.R. Ortiz-Longo,[1]* K.W. White,* and C. Vipulanandan†
*Department of Mechanical Engineering, University of Houston, Houston, TX, USA
†Department of Civil & Environmental Engineering, University of Houston, Houston, TX, USA

(Received April 14, 1998; in final form July 10, 1998)

ABSTRACT

The influence of sand grain size on the bridging stress-crack opening displacement curve has been investigated by the Post Fracture Tensile (PFT) testing technique. The PFT method is a well-established technique used in studies of wake-toughened ceramic systems. This method isolates and characterizes the role of microstructure in the development of closure stresses in the process zone. The critical stress was found to be higher for the coarse-grained specimen, but there was no influence of the sand grain size on the critical crack opening displacement. The stress-displacement curves, grain size distribution data, and SEM observation of the fracture surfaces suggest that the coarse sand grains are not very efficient in bridging the crack front and consequently give a negligible contribution to the load sharing event in the wake zone. © *1998 Elsevier Science Ltd*

Introduction

Recent attention in the field of fracture mechanics of cementitious and ceramic materials has addressed the role of the wake process zone in the toughening characteristics, as evidenced by a rising R-curve behavior. A quantitative evaluation of the distribution and magnitude of the cohesive stresses transferred within the process zone and the microstructural mechanisms affecting them is of great importance in understanding the fracture processes in these materials. Several indirect methods have been proposed to characterize the relationship between the bridging stresses and the crack opening displacement (COD) in the wake zone based on experimental observations and theoretical models. Hillerborg et al. (1), proposed the existence of cohesive stresses which varied linearly with crack separation, having a maximum stress at the point of minimum crack separation.

Wecheterana and Shah (2) applied a similar concept to model the post peak response in fiber-reinforced concrete according to the relationship:

$$\frac{\sigma}{\sigma_{max}} = \left(1 - \frac{u}{u_{max}}\right)^{m} \tag{1}$$

[1]To whom correspondence should be addressed.

where u is the crack opening displacement, σ is the post-cracking stress, and m is the strain-softening exponent equal to two.

Mai and Lawn (3) and Foote et al. (4) adopted the same power-law function (Eq. 1) for ceramic and cementitious materials and characterized the exponent m according to the different types of cohesive stresses existing in various kinds of materials. They suggested an $m = 0$, for a uniformly distributed stress over the bridging zone, $m = 1$ for frictional pullout of the bridging grains, and $m = 2$, for fibrous composite materials.

Wittmann and Hu (5–7), and Wittman (8) introduced a feasible experimental method to estimate the extent of the fracture process zone and the distribution of the bridging stresses within it. This comprised of step-wise renotching of an extended crack and measuring the change in compliance between each saw-cut until the modified compliance reached the linear-elastic value upon complete removal of the wake. A similar technique was adapted by Knehans and Steinbrech (9) and Grimes et al. (10) for ceramics to indicate the predominant contribution of the trailing wake region (behind the crack tip) rather than the frontal zone to the rising R-curve behavior.

There have also been several efforts toward the experimental determination of the strain-softening relationship (11–17). Gopalarathnam and Shah (13), attempted to experimentally identify the softening response of plain concrete in tension using double-edge-notched beam specimens. In situ optical observations revealed that a single crack formed across the specimen width just after the peak load. Assuming zero crack width at peak stress level, they analytically modeled the post-peak strain-softening response. A similar technique was used by Cornellisen et al. (14), to determine fracture mechanics parameters in normal and lightweight concrete. Li et al. (18), suggested an indirect method to experimentally determine tension-softening curves in mortar using the J-Integral concept.

Reichl and Steinbrech (19) experimentally measured the average load carrying capacity of the wake due to bridging forces in ceramic specimens using a short DCB specimen with a small backnotch. This work only considered one stress evaluated from one COD condition. But, the bridging stresses actually decay rapidly with increasing crack face separation due to the reduction in the number of active grains bridging the larger CODs. In Figure 1, a schematic illustrates the decreasing stress with increasing COD. In a method proposed by Hay and White (20–22), Post-Fracture Tensile (PFT) specimens were cut from behind the crack tip of a damaged DCB specimen and the isolated sections were loaded in tension to obtain the bridging stress distribution as a function of increasing COD behind the crack tip. From the PFT results, a COD/Grain-Size (β) criterion was evaluated, which quantifies the efficiency of the bridging grains in carrying loads within the wake region. Application of the PFT technique to DCB specimens provide a link to R-curve characterization methods (22).

There have been several studies to correlate the relationship between the mechanical behavior of concrete and the microstructure of the interfacial zone between the cement paste and the aggregate (23,24). The chemical and mineralogical aspects of the microstructure have also been extensively reported in the literature (25–27). It is widely believed among authors that the interface between the cement and the aggregate is the weakest region in the matrix due to its enhanced porosity and controls the fracture process significantly. However, the effect of the physical nature of the interface on the grain pull-out process in the wake zone has not been referenced in the literature in any great detail. To better characterize the softening response of cement mortars, characterized by the grain bridging processes, one seeks to measure the bridging stresses directly as a function of crack-opening displacements and correlate this response with the structure of the cement mortar.

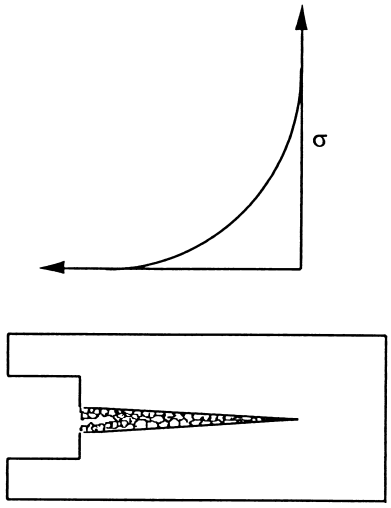

FIG. 1.
Schematic view of the grain-bridging mechanism.

The present approach is a novel application of the Post-Fracture Tensile (PFT) technique to wake zone characterization of cementitious materials. This will lead to a better understanding of the detailed mechanisms controlling the wake-zone toughening process. The bridging stresses are directly correlated to the microstructural constituents such as aggregate size and morphology and physical nature of the aggregate-cement matrix interface in mortar specimens.

Materials and Methods

The mix proportions of the mortar used in this study are given in Table 1. The cement mortar was cast in 150 mm × 51 mm × 25 mm plate form and cured in a humid room

TABLE 1
Material composition of mortar.

Cement type	Portland cement
Aggregate type	Blasting sand FG (0.6 mm nominal grain size) CG (1.1 mm nominal grain size)
Water/cement ratio	0.4
Cement:sand (by weight)	1:2
Curing time	21 days
Unit weight	20.6 KN/m^3

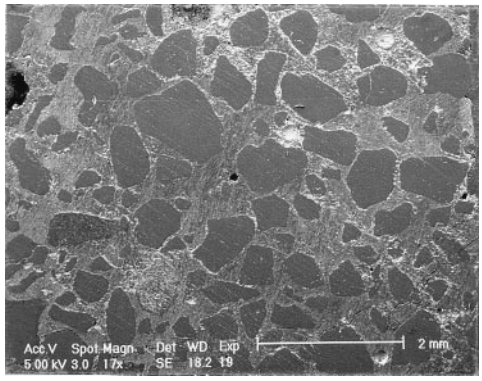

FIG. 2.
Polished sample of the fine-grained mortar specimen.

(100% relative humidity at 23°C) for nominally 21 days resulting in a mortar of 20.6 KN/m^3 unit weight. Two types of mortar specimens with different sizes of sand were chosen for the study and coded as FG (fine grained) and CG (coarse grained) as indicated in Table 1.

Polished samples of the fine-grained and coarse-grained mortars, shown in Figure 2 and Figure 3 respectively, indicate the size morphology and spatial arrangement of the grains. Specimens were prepared for the optical micrographs by polishing with coarse to fine silicon carbide paper on a Vibromet wheel with a final polish with 5 μm diamond paste. The average aggregate size for the FG specimen determined from Figure 2 was 550 μm and that of the CG sample determined from Figure 3 was approximately 1200 μm.

The DCB specimen geometry was selected for testing for two reasons. First, the small COD profile required for the PFT test is more easily obtained from a long crack than from the short crack associated with a bend bar (28,29). Secondly, the R-curves for the bend-bar

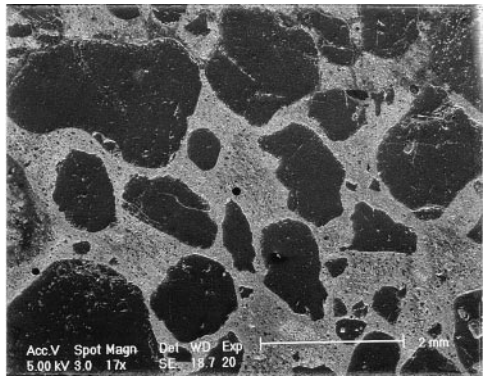

FIG. 3.
Polished sample of the coarse-grained mortar specimen.

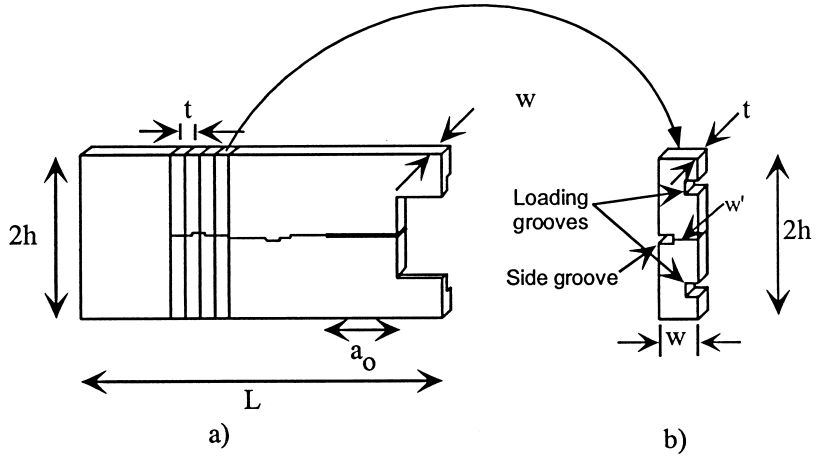

FIG. 4.
Schematic of DCB and PFT specimen. *a*) Fractured DCB. *b*) PFT specimen.

specimens are sensitive to initial crack (29). The DCB specimens were cut with a diamond slicing blade with a hydraulically driven surface grinder from the above plates where the specimen dimensions are (Fig. 4) $L = 145$ mm, $a_o = 50.8$ mm, $h = 25.2$ mm, $w = 12.7$ mm, $w' = 6.35$ mm, and $t = 3.81$ mm.

A side groove (only shown in Fig. 4b for clarity) was introduced to ensure that the crack remained in plane. Two sets of DCB and PFT tests were performed for each of the FG and CG samples.

The fracture tests were carried in the Universal load frame (Instron Corporation, Canton, Mass.) using a cross-head speed of 2.5 m/min. Upon completion of the fracture test, the crack tip location was confirmed using an optical microscope. The crack length typically fell between 35–40 mm. Load-displacement records were used to determine elastic-equivalent crack lengths by the compliance technique. The stress intensity factors for crack extension were evaluated as a function of crack length by (30,31):

$$K_{R_i} = P_i a_i \frac{Y_i}{\sqrt[3]{(bh)^2}}$$

where P_i is the instantaneous load, a_i is the corresponding crack length, b is the effective thickness (32) given by parameter $\sqrt{ww'}$, and h is the specimen height.

In addition to the crack-stabilizing side groove in the DCB specimens, two parallel grooves were machined. These grooves accommodate the PFT loading fixtures, such that the load points align with the center of the cracked ligament. Thin slices, 3.81 mm thick, were extracted from the wake region (as indicated in Fig. 4) to form the PFT specimens. The DCB specimen was secured to a steel substrate using a thermal glue (brittle at room temperature) to avoid damage to the wake during the slicing step. Since the peak stress and stiffness of a PFT curve depends on initial CODs, the starting crack face separation was measured for all PFT specimens in an optical microscope.

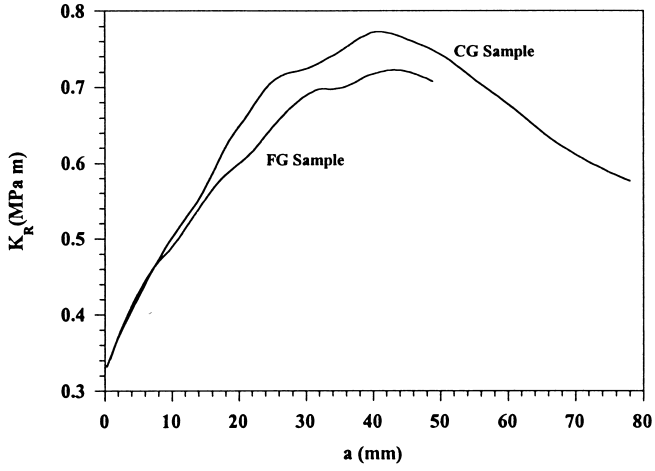

FIG. 5.
Resistance curves (K_R) evaluated from load-displacement data of DCB fracture test.

Results and Discussion

The K_R data were compiled from the load displacement data obtained from the DCB tensile tests and have been shown in Figure 5, for both the FG and CG specimens. The KR data can be represented as the sum of a crack tip component and a wake component, given by

$$K_R = K_i + \Delta K$$

where K_i is the initial point on the R-curve representing the crack tip resistance and ΔK is the shielding component due to the wake zone tractions. The point on the R-curve where the K_R values plateau indicates a fully saturated bridging zone which travels with the crack tip. Figure 5 indicates that there is no noticeable difference in the bridging zone length for the CG and FG samples, but the "ΔK" toughening component for the CG specimen was slightly higher than that of the FG specimen. In general, the shielding component for both the mortar specimens was quite low when compared with other materials like structural ceramics (22). This indicates a significantly lower grain bridging efficiency for these materials, as grain bridging is a characteristic constituent of the toughening component.

PFT specimens were loaded in tension at a cross-head speed of 2 μm/min to obtain load-displacement data. The load was divided by the cross-sectional area of the fractured region of the PFT specimen to obtain bridging stresses and the initial displacements were shifted to account for the residual CODs from the DCB fracture test.

A typical stress-displacement data from a PFT test is shown in Figure 6. The stress-displacement curve contains four behavioral regions where the response is distinctly different. An apparent linear elastic region characterizes the behavior for loads below approximately 90% of the maximum value, suggesting that only minor non-recoverable contributions to the deformations are participating. Just prior to the maximum load, a short non-linear region indicating non-recoverable grain activity exists. Beyond the maximum

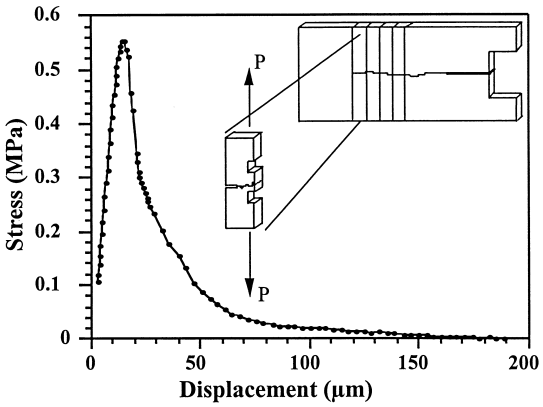

FIG. 6.
Typical PFT stress-displacement curve for the fine-grained mortar.

load, the load bearing capacity of the process zone decreases monotonically due to the increased crack-face separation ultimately reaching a negligible, but constant load.

The COD profile increases from zero at the crack tip to a maximum at the crack mouth close to the chevron notch. The grain-bridging efficiency is quantified in this study by the COD/grain size criteria (β), which indicates the amount of physical overlap required for measurable bridging, and is shown schematically in Figure 7. The grains which satisfy the COD/grain size criteria participate in the load sharing event, provided there is no detrimental effect from the aggregate-matrix interfacial zone, and are referred to as the active grains. The increase in COD away from the crack-tip leads to a decrease in the number of active grains as the smaller size fractions can no longer take part in the load sharing event. Hence, bridging is a maximum at the crack tip and minimum at the crack mouth. From this analysis, it is evident that the distribution of tractions in the wake zone depends on the grain size.

To study this behavior in more detail, various PFT specimens with different starting CODs

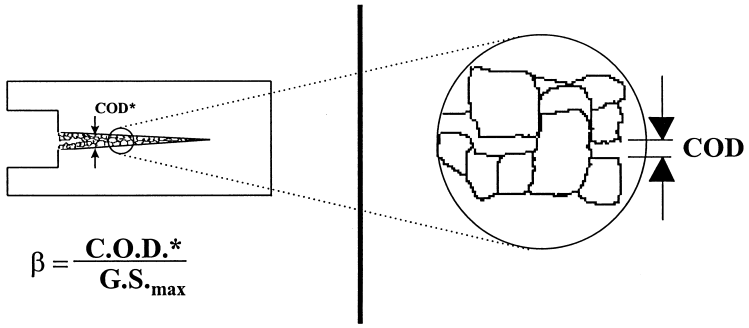

FIG. 7.
Schematic view indicating the physical significance of the bridging efficiency factor, β. Here, negligible loads may be carried by grains even though overlap is apparent.

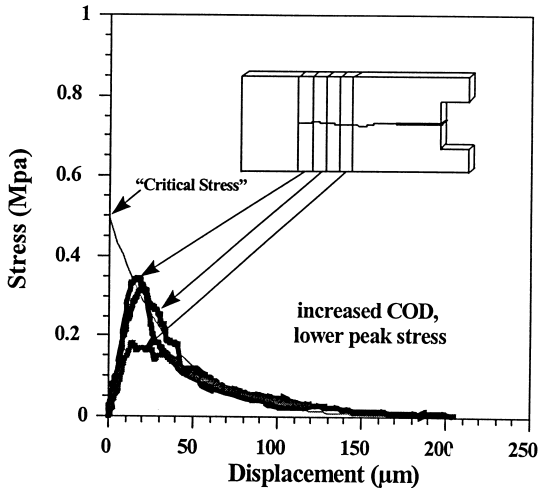

FIG. 8.

Family of PFT stress-displacement curves for the fine-grained specimen with different initial CODs. A curve-fit to the envelope described by the curve family estimates the stress-displacement relationship.

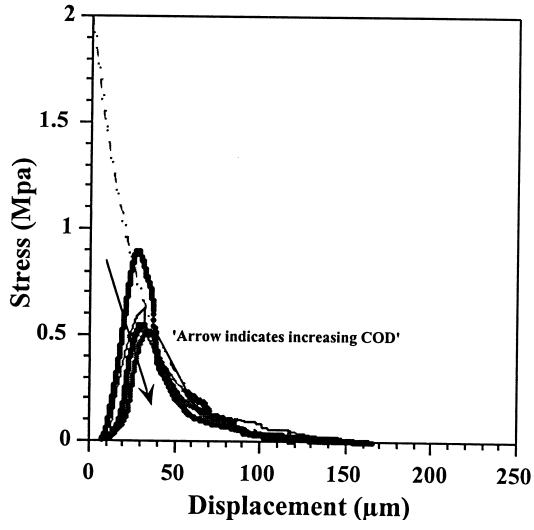

FIG. 9.

Family of PFT stress-displacement curves and its curve-fit for the coarse grained mortar specimen.

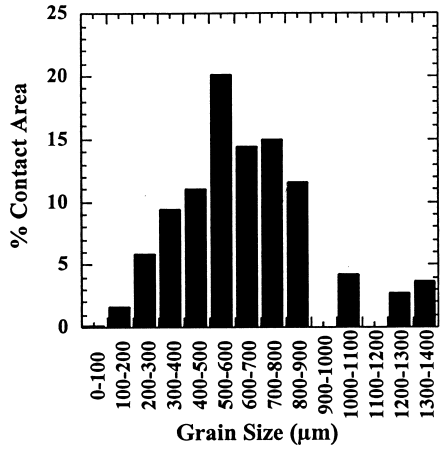

FIG. 10.
Grain size distribution for the fine-grained mortar specimen.

were tested in tension for both the FG and the CG samples. Three such PFT results for the FG sample are shown in Figure 8. The lower curve corresponding to the largest COD profile (farthest from the crack-tip), indicates the lower bridging stresses as a result of the smaller number of active bridging grains. The greater damage caused by the larger COD results in a reduction of elastic stiffness and peak stress. With reduction in starting COD, the improved contact of the active bridging grains results in higher peak stresses and elastic stiffness, as shown by the higher curves. The reasonably good agreement between the falling tail portions of the PFT curves, signifies that the bridging stresses in the fracture process zone are characteristic of the microstructure and the grain size distribution of the mortar specimen.

A curve-fit to the envelope described by the family of PFT curves is also shown in Figure 8. The stress axis intercept of this curve-fit gives an indication of the critical stress (the fictitious stress required to separate a crack with zero COD, but in which the chemical bonds have been broken). This extrapolated curve-fit describes the crack-closure stress-COD relationship. For the FG sample this yields a critical stress (σ^*) of 0.5 MPa and a critical COD of around 120 to 130 μm.

Four PFT results for the CG sample are shown in Figure 9 along with the extrapolated bridging stress-COD curve-fit. For this mortar specimen, the results indicate a σ^* value of around 2 MPa and a critical COD (u^*) of around 110 to 120 μm. From these values, it is evident that the coarse-grained specimen when compared to the fine-grained one has higher values of bridging stresses at very small CODs, but there is a significantly sharper drop in the closure stresses during the entire pull-out process for the coarse-grained specimen.

Microstructure and Grain Size Distribution

The grain size distribution of the mortar samples considered in this study was determined from polished samples. All grains were characterized for their long and short dimensions from optical micrographs (e.g., Figs. 2 and 3) and the grain area was calculated assuming the

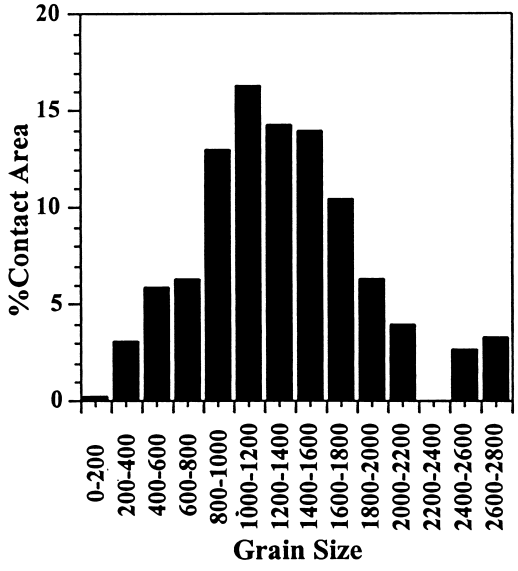

FIG. 11.
Grain size distribution for the coarse-grained sample.

grains to be elliptical. The grain sizes reported are the equivalent diameters of these elliptical grains with the same cross-sectional area. The grain sizes are categorized in 100 μm intervals for the FG sample (Fig. 10) and 200 μm intervals for the CG sample (Fig. 11). To relate the effects of grain size to stress-displacement curves, the area fraction occupied by each grain size category has been plotted. For the FG sample, the majority of the area is occupied by

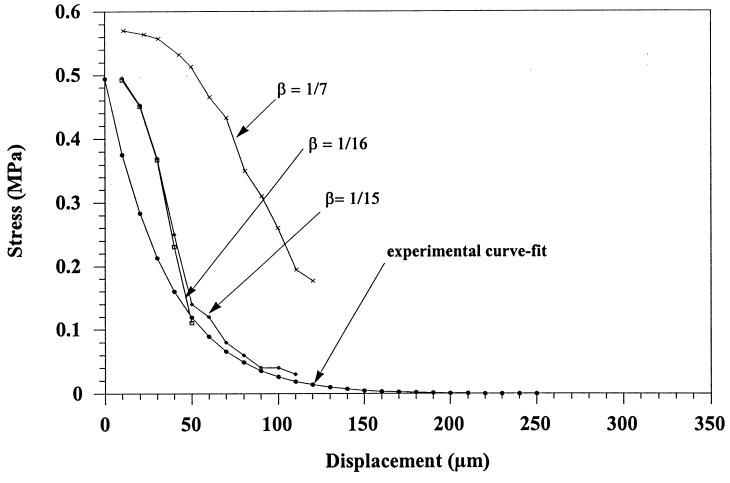

FIG. 12.
Stress-displacement curves modeled from grain size distribution and the power-law curve-fit for the FG sample.

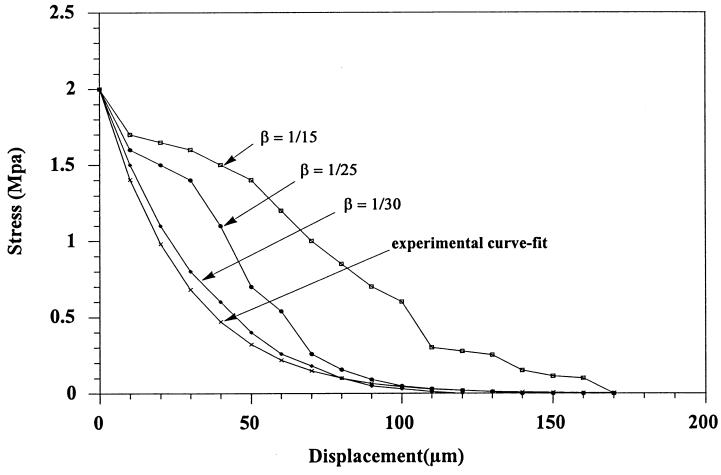

FIG. 13.
Modeled stress-displacement curves and power-law curve-fit to experimental data for the CG sample.

grains ranging from 300 μm to 900 μm in diameter with an average grain size of approximately 550 μm. For the CG sample, the maximum area is occupied by grains in the 800 to 2000 μm category and the average grain size is approximately 1200 μm.

The microstructural influence on the stress-displacement curve was analyzed by assessing a COD/grain-size (β) criterion, which is quantified by the amount of physical overlap required for grain bridging. An assumption is made that the same β factor applies to all grain sizes within the same microstructure (FG or CG). The active area fraction (area fraction occupied by active grains satisfying the β criteria), was calculated by integrating the data in Figures 10 and 11 from "1/β" times the COD to the maximum grain size. Repeating this for

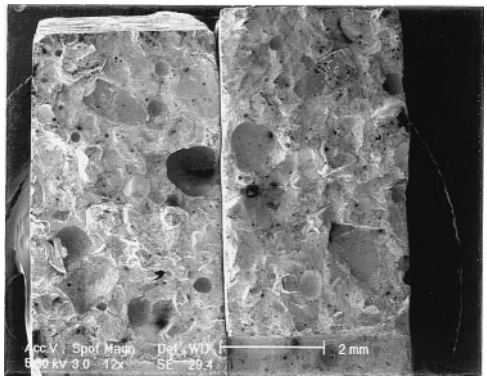

FIG. 14.
Fractographs of mating fracture surfaces of the fine-grained specimen.

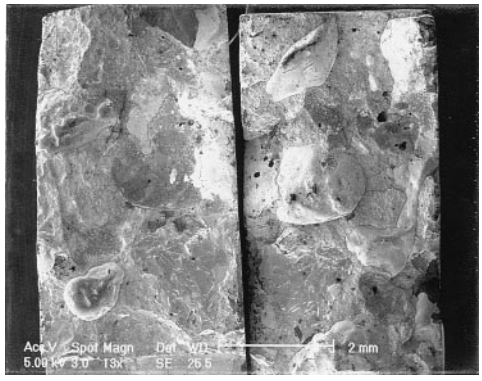

FIG. 15.
Fractographs of mating fracture surfaces of the coarse-grained sample.

the entire range of CODs results in a relationship describing the active contact area versus displacement which is then multiplied by the critical stress value (0.5 MPa for FG and 2 MPa for the CG sample). This leads to a modeled PFT stress displacement relationship as shown in Figure 12 and Figure 13. Comparison of the modeled curves with the experimentally determined PFT curve-fits shows that a "β" value of 1/15 to 1/16 gives a good curve fit for the FG specimen and a corresponding value of 1/30 gives good agreement for the CG specimen. This signifies a much lower grain bridging efficiency for the CG mortar sample.

Figure 14 and Figure 15 show the fractographs from mating surfaces of the FG and CG samples, respectively. The fracture surface of both the samples show a predominantly inter-granular fracture, where grain pull-out has occurred from mating sockets. A salient feature is that the degree of tortuisity and roughness in the CG sample fracture surface is less than that of the FG sample. There is also some evidence of transgranular cleavage of the very

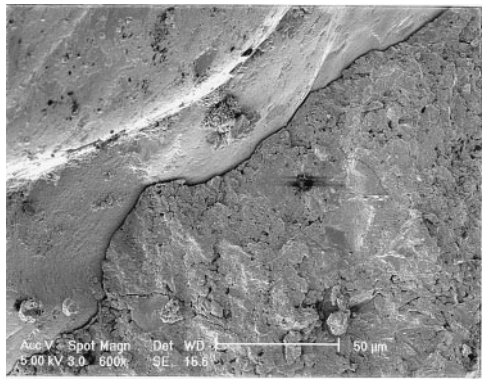

FIG. 16.
Paste-aggregate interface for a fine-grain size sand aggregate showing a dense structure from where pull-out has taken place (cured sample).

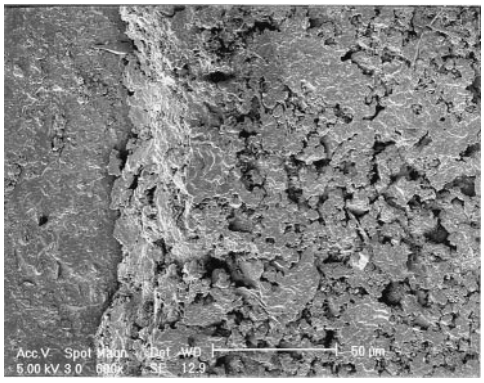

FIG. 17.
Paste-aggregate interface for a very coarse sized aggregate showing a porous and open structure (cured sample).

coarse grains in the fractographs. This indicates that in the fine-grained sample, almost 100% of the grains can participate in the load sharing event, provided they meet the COD/grain size criteria, whereas the very large grains in the coarse grained microstructure which have failed due to cleavage cannot contribute to the bridging stresses. The greater relief in the fine-grained fracture surface supports the higher interlocking parameter computed from the PFT results and grain size distribution data for this specimen. The increased pull-out distance characteristic of the FG microstructure may result from the more tortuous crack path. However, in both of the fracture surfaces, it is seen that the separation of some of the sand grains occurred preferentially within the cement paste, leaving hydrated cement matrix material at the aggregate side of the specimen as shown in Figures 16 and 17. This indicates that the nature and physical characteristics of the duplex film (CH and CSH) (26,34), bulk

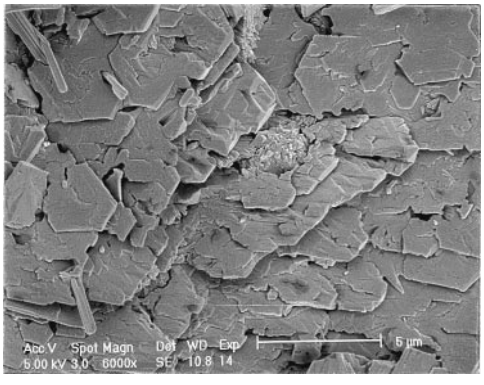

FIG. 18.
Morphology of the paste side of the fine aggregate-matrix interface showing $Ca(OH)_2$ platelets (cured sample).

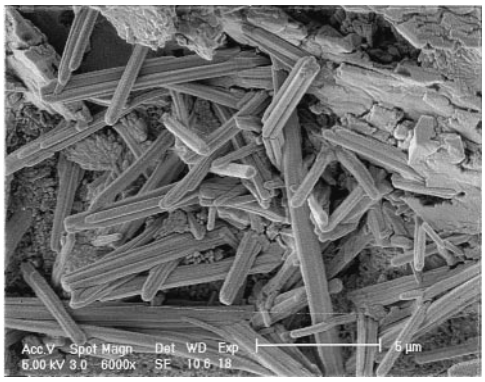

FIG. 19.
Aggregate surface containing needle-like crystals of ettringite (cured sample).

cement paste at regions close to the interface and the film-cement paste interface is important in determining grain pull-out behavior. Hadley (35) reports that fracture rarely occurs at the true paste-aggregate interface. However, for longer times of curing, fracture takes place almost in the immediate vicinity of the paste-aggregate interface and sometimes through the interfacial film.

To examine the influence of the size of the aggregate particles on the physical nature of the interface, the mating sockets from where aggregates have pulled out were observed under the SEM as shown in Figures 16 and 17 for the fine and coarse grain aggregates, respectively. It is clearly evident that the degree of porosity in the coarse aggregate-cement interface is higher than that for the finer aggregates. The reason for this highly open structure under coarse aggregates is that bleed water dwells under the coarse sand particles and creates a locally high water-to-cement ratio during sedimentation and settling of the cement paste in unhardened cement mortar. The "wall effect" as described in the literature (23,36), is obviously greater for the coarse aggregates than for the finer ones and hence it is expected that the local water-to-cement ratio is higher for regions under the coarser sand particles. The relatively smaller open space in the fine aggregate interfaces may be filled up by hydration products such as hexagonal plate-like CH crystals occurring in packets or booklets (see Fig. 18), at later stages of hydration. Similar features have also been reported by other authors (26,35). A thin continuous film of $Ca(OH)_2$ without identifiable crystallites was also formed in some areas of the interface. This type of morphology of the hydration products result in a dense interfacial structure near the fine sized aggregates, which is effective in rendering high sliding friction during grain pull-out. In contrast, the higher local water-to-cement ratio at the interfaces of the very coarse particles create larger void spaces, which cannot subsequently filled with the CH platelets. As a result, some of the interfaces show a loose network of hydrated cement grains (5–10 μm in size) on which needle-like crystals of ettringite have developed. Some of these hydration products are shown in Figure 19. The interface of some of the coarse-sized aggregates in the CG sample show evidence of partial development of the dense $Ca(OH)_2$ platelets similar in morphology as those seen in Figure 18.

The highly porous structure of the coarse aggregate-matrix interface is responsible for the low sliding frictional coefficient during the pull-out of the debonded grains. As sliding friction is the

main component of the closure/bridging stresses existing in the post-fracture specimens during the tensile test (37), this type of structure reduces the load carrying capacity of the very large sand grains. This phenomenon explains the sharp drop in the bridging stress-COD curve for the coarse aggregate structure and a consequent reduction in the overall bridging efficiency.

The higher critical stress for the coarse-grained specimen can be explained by analyzing the grain size distribution of the two varieties of sand samples. In the CG sample, observations of the nature of porosity in interfacial regions and the mechanical response lead us to believe that aggregates ranging in size up to around 1400–1600 μm effectively take part in the grain bridging process. The more coarse aggregates have an almost negligible contribution to the load-bearing capacity of the wake due to the nature of the underlying interface and transgranular fracture. However, the grain size distribution shows that the total contact area of grains up to the above size range is much larger for the coarse-grained structure (see Figs. 12 and 13). This leads to very high bridging stresses for this type of microstructure at low crack-opening displacements, as a larger area of active grains can participate in the pull-out process.

The grain bridging efficiency factor, β, of the coarse-grained microstructure, computed by integrating the grain size distribution data up to the maximum active size range of 1400 to 1600 μm, was 1/20 to 1/21. The higher size ranges were not taken into consideration due to their negligible contribution to the bridging process because of the detrimental effect of the coarse aggregate-matrix interface. The closer agreement of the β value for the CG specimen calculated in this manner to that for the FG specimen, supports the argument that in the particular coarse-grained microstructure studied, sand grains up to the above specified size range can efficiently take part in the bridging activity and the nature of the interface plays a critical role in impairing the bridging efficiency the very coarse sand grains.

Overall Summary and Conclusions

Cement mortar of unit weight 20.6 KN/m^3 was studied. The following conclusions are submitted for the model of mortars investigated:

1. The Post Fracture Tensile (PFT) technique has been used successfully as an experimental tool to directly measure the grain bridging stresses in the wake zone of the mortar specimens. The reasonably good agreement between the falling portion of the stress-COD curves from PFT specimens obtained from a single DCB specimen authenticates the above statement that the microstructure and grain size distribution of cementitious materials have a critical influence on the strain-softening behavior.
2. The mechanical response of fine-grained mortar (average size 0.6 mm) was distinctly different from of coarse grain sand (average size 1.1 mm). Although the critical stress of the CG sample was higher than the FG, there is no noticeable difference in the critical COD of the above samples. The grain bridging efficiency of the coarse-grained microstructure was computed to be much less than that of the fine-grained one.
3. There is some contrast in the degree of roughness in the fracture surfaces of the FG and CG samples. This may be partly responsible for the difference in the grain bridging efficiency of the fine and coarse aggregates. Another significant observation was the difference in the degree of porosity in the aggregate-matrix interfacial regions of the fine and coarse sand grains. The highly porous and open structure developed under very coarse aggregates, due to possible bleeding effects, results in poor frictional pull-out of

these particles and consequently make them ineffective in the wake-zone load sharing event. This explains the sharp drop in the wake stresses of the CG sample at higher CODs.

References

1. A. Hillerborg, M. Modeer, and P.E. Petersson, Cem. Concr. Res. 6, 773 (1976).
2. M. Wecheterana and S.P. Shah, Cem. Concr. Res. 13, 819 (1983).
3. Y.W. Mai and B.R. Lawn, J. Amer. Ceram. Soc. 70, 289 (1987).
4. R.L. Foote, Y.W. Mai, and B. Cottrell, J. Mech. Phys. Solids 34, 593 (1986).
5. F.H. Wittmann and X. Hu, J. Mater. Civ. Eng. 2, 15 (1990).
6. F.H. Wittmann and X. Hu, Int. J. Fract. 51, 3 (1991).
7. F.H. Wittmann and X. Hu, Cem. Concr. Res. 21, 1118 (1991).
8. F.H. Wittmann, Fracture Mechanics of Concrete, Z.P. Basant (ed.), p. 392, Elsevier, New York, 1992.
9. R. Knehans and R. Steinbrech, J. Mater. Sci. Let. 1, 327 (1982).
10. R.E. Grimes, G.P. Kelkar, L. Guazzone, and K.W. White, J. Am. Ceram. Soc. 73, 1399 (1990).
11. P.H. Evans and M.S. Marathe, Mater. Struct. (RILEM) 1, 61 (1968).
12. O. Peterson, Report TVBM-1006, Division of Building Materials, Lund Institute of Technology, Lund, Sweden (1981).
13. V. Gopalaratnam and S.P. Shah, ACI J. 82, 310 (1985).
14. H.A.W. Cornellisen, D.A. Hordijk, and H.W. Reinhardt, Fracture Toughness and Fracture Energy of Concrete, F.H. Wittmann (ed.), p. 565, Elsevier, New York, (1986).
15. J.G.M. Van Mier, Cem. Concr. Res. 21, 545 (1991).
16. N. Nomura, H. Mihashi, and M. Izumi, Cem. Concr. Res. 21, 545 (1991).
17. T. Steiger, H. Sadowski, and F.H. Wittmann, Proceedings of Fracture Mechanics of Concrete Ceramics, Vol. II, p. 157, F.H. Wittmann (ed.), Aedificatio Publishers, Germany, 1995.
18. V.C. Li, C.M. Chan, and C.K.Y. Leung, Cem. Concr. Res. 17, 441 (1987).
19. A. Reichl and R.W. Steinbrech, J. Am. Ceram. Soc. 71, C299 (1988).
20. J.C. Hay and K.W. White, Acta Met. Mat. 40, 3017 (1992).
21. J.C. Hay and K.W. White, J. Am. Ceram. Soc. 76, 1849 (1993).
22. J.C. Hay and K.W. White, J. Am. Ceram. Soc. 77, 2283 (1994).
23. K. Mitsui, Z. Li, D.A. Lange, and S.P. Shah, ACI Mater. J. 91, 30 (1994).
24. Y. Kosaka and F. Tanigawa, J. Arch. Inst. Japan 228, 1 (1975).
25. F.H. Wittmann, Fracture Mechanics of Concrete, p. 43, Elsevier, Amsterdam, 1983.
26. B.D. Barnes, S. Diamond, and W.L. Dolch, Cem. Concr. Res. 8, 223 (1978).
27. C. Tasedemir, T.A. Tasedemir, R. Grimm, and G. Konig, Proc. of the 2nd. Int. Conference on Fracture Mechanics of Concrete Structures (FramCOS 2), p. 125, Aedificatio Pub., Freiburg, Germany, 1995.
28. R.W. Steinbrech, R. Knehans, and W. Schaarwachter, J. Mater. Sci. 18, 265 (1983).
29. R.W. Steinbrech, F. Deuerler, and A. Reichl, Sci. Ceram. 14, 656, (1988).
30. G.P. Kelkar. University of Houston; M.S. Thesis. 1989.
31. M.F. Kanninen, Int. J. Fract. 10, 415 (1974).
32. J.E. Srawley and B. Gross, Mat. Res. Stand. 7, 155 (1967).
33. G. With, J. Am. Ceram. Soc. 72, 710 (1989).
34. L. Strumble, Bonding in Cementitious Composites, p. 11, MRS Publications, Pittsburg, PA, 1987.
35. D.W. Hadley. Purdue University; Ph.D. Thesis. 1972.
36. P.K. Mehta, P.J.M. Monteiro, Bonding in Cementitious Materials, p. 65, Research Society Pub., Pittsburgh, PA, 1987.
37. S.J. Bennison, B.R. Lawn, Acta Met. 37, 2659 (1989).